Materials Advances

ROYAL SOCIETY OF CHEMISTRY

PAPER

View Article Online
View Journal | View Issue

Cite this: *Mater. Adv.*, 2026, 7, 976

Selected sustainably synthesized metal–organic frameworks for hydrogen and carbon dioxide storage

Nejat Redwan Habib,[ab] Isabel Diaz,[c] Abi M. Taddesse[d] and Henrietta W. Langmi*[a]

Selected metal–organic frameworks (MOFs) including Al–MIL-53–NH_2, Fe–MIL-100, Zr–BDC and Zr–BDC–NH_2 were synthesized *via* a sustainable approach and tested for hydrogen and carbon dioxide storage. The synthesis was conducted at room temperature in the presence of water acting as a solvent. Crystalline Fe–MIL-100, nanocrystalline Al–MIL-53–NH_2, and semi-crystalline Zr–BDC and Zr–BDC–NH_2 were formed as confirmed by powder X-ray diffraction. Fourier transform infrared spectroscopy further confirmed the successful metal–ligand coordination in the MOFs. Thermogravimetric analysis shows that Zr–BDC was the most stable among the synthesized MOFs as it started to decompose above 500 °C. Morphological evaluation using field emission scanning electron microscopy reveals that Fe–MIL-100 consisted of octahedral-shaped crystals while Al–MIL-53–NH_2, Zr–BDC and Zr–BDC–NH_2 manifested as agglomerated particles. The agglomeration, further validated by transmission electron microscopy, results from the clustering of nanocrystals or small particles. This occurs due to the rapid formation of the precipitate during the room-temperature synthesis, where water serves as the solvent for the specified MOFs. The highest Brunauer–Emmett–Teller (BET) surface area (2013 $m^2\ g^{-1}$), determined from nitrogen sorption, was recorded for Fe–MIL-100. Accordingly, Fe–MIL-100 exhibited the highest H_2 uptake (1.0 wt% at 77 K and 1 bar) and CO_2 storage (8.5 wt% at 298 K and 1 bar). This study illustrates the potential of certain sustainably produced MOFs for gas storage applications. Sustainably prepared MOFs provide the benefit of scalable synthesis suitable for industrial production by reducing reaction times and employing environmentally friendly solvents.

Received 16th July 2025,
Accepted 22nd November 2025

DOI: 10.1039/d5ma00763a

rsc.li/materials-advances

1. Introduction

A large amount of energy utilized by humans is derived from fossil fuels, such as natural gas, oil and coal, which has raised significant environmental problems.[1] Carbon dioxide (CO_2), released from burning of these carbonaceous substances and other industrial activities, is a major greenhouse gas. The rise in atmospheric concentrations of CO_2 enhances the greenhouse effect that holds heat near the Earth's surface, leading to climate change.[2] To address these issues, efficient CO_2 capture and clean energy source alternatives are necessary. Solar, wind, hydropower, nuclear and hydrogen are alternatives to non-fossil fuel-based energy systems.[3,4] Hydrogen (H_2) has been studied as a promising energy carrier because of its high energy density per unit mass and its environmentally friendly characteristics, including zero carbon emissions during power generation. However, its volumetric energy density, or energy per unit volume, is low under standard conditions. To address this issue, research is concentrated on developing gas storage materials that are both efficient and cost-effective. Nonetheless, achieving efficient storage and release of gas remains a significant challenge and continues to be an area of active research.[1] CO_2 and H_2 can be stored in materials either by a chemical or physical adsorption process. Physical adsorption, where gases adsorb onto porous materials, has signified great potential due to the relatively fast kinetics in the adsorption and release of gases.[5] In this regard, porous materials such as zeolites,[6] porous carbon[7] and metal–organic frameworks (MOFs) are being studied as favorable porous materials for gas sorption.[8] The physiochemical properties of MOFs, including high porosity and surface area, tunable pore size, and stability, together with their diverse structures, have led to their intensive exploration as gas storage materials.[9–11]

[a] *Department of Chemistry, University of Pretoria, Private Bag X20, Hatfield, 0028, South Africa. E-mail: henrietta.langmi@up.ac.za*
[b] *Department of Chemistry, Adama Science and Technology University, Adama, Ethiopia*
[c] *Instituto de Catálisis y Petroleoquímica, ICP-CSIC. C/Marie Curie 2, 28049, Madrid, Spain*
[d] *Department of Chemistry, Haramaya University, Dire Dawa, Ethiopia*

The synthesis of MOF materials for gas storage has predominantly been performed using hydrothermal and solvothermal synthesis approaches.[12,13] These conventional MOF synthesis techniques prevalently produce well-assembled MOFs with good quality crystals and morphology.[14] However, high energy consumption, prolonged durations of synthesis and environmentally unsuitable solvents are used for the conventional synthesis of MOFs. These factors limit their application in industrial-scale production. On the other hand, synthesizing MOFs at room temperature in water is a cleaner option.[12,15] The water solvent and room temperature synthesis approach can decrease the cost. This is crucial to initiate industrial-scale MOF production.[15,16] As such, in previous studies, sustainably synthesized MOFs were applied for photocatalysis[15] and for the removal of bisphenol A.[17] Also, the use of surfactants on sustainably synthesized MOFs to introduce mesoporosity in the MOFs, and to change the crystal size was studied.[17,18]

In the current study, iron-based MIL-100, aluminium-based MIL-53–NH_2, and zirconium-based UiO-66 family MOFs (specifically Zr–BDC and Zr–BDC–NH_2) are the chosen MOFs of interest to investigate H_2 and CO_2 gas storage. The major criterion for the selection of MOFs is their ability to be synthesized at room temperature in water. Furthermore, the selected MOFs have independent characteristics, which make them suitable for gas storage applications. The breathing effect of the Al–MIL-53 MOF, characterized by its ability to reversibly adjust pore sizes in response to guest molecules, makes it a subject of extensive research for gas uptake and release.[19] The amino functional groups in the Al–MIL-53–NH_2 MOF are reported to have an advantage in forming interactions with gases, resulting in high uptake of gases such as CO_2.[20] The high abundance, reduced toxicity and versatility make Fe-based MOFs a preferred choice as gas adsorption materials.[21,22] In addition, the Fe–MIL-100 MOF is known to have a high surface area with small mesoporous cavities, which can increase the physical adsorption of gases.[23] The tetra valent zirconium MOFs with oxygen ligands are robust materials with a large window size that enhances the diffusion of gases during gas sorption.[24,25] The presence of amino groups in amino-functionalized zirconium MOFs increases the interaction of MOFs with gas molecules.[20,26,27]

The cost-effective and environmentally safe synthesis of MOFs will pave the way for scalable industrial production of these materials in the gas storage sector. In this work, MOFs specifically Fe–MIL-100 and Al–MIL-53–NH_2 as well as Zr–BDC and Zr–BDC–NH_2 were synthesized employing a sustainable method. The synthesized MOFs were characterized and tested for H_2 and CO_2 storage at low pressure.

2. Experimental

2.1. Synthesis of Al–MIL-53–NH_2

The synthesis of Al–MIL-53–NH_2 was carried out *via* a sustainable method at room temperature in water.[17,28] Accordingly, Beaker 1 contained 1.45 g $AlCl_3{\cdot}6H_2O$ (Sigma-Aldrich, 99%) that was added to 3 mL of H_2O to form a solution. In Beaker 2, 1.09 g 2-amino terephthalic acid (NH_2–H_2BDC, Sigma-Aldrich, 99%) was added to 13.05 mL of 1 M solution of NaOH. NaOH served as a deprotonating agent of organic linkers to make water-soluble salts of the linkers. The Al metal salt solution in Beaker 1 was added slowly to Beaker 2 containing the linker solution while stirring. The immediately formed yellow precipitate was left for 24 h under stirring. Thereafter, washing of the precipitate was carried out with water and ethanol (3×) and the product was left to dry at room temperature.

2.2. Synthesis of Fe–MIL-100

The sustainable synthesis of Fe–MIL-100 was performed based on an established method.[23] Beaker 1 contained 2.27 g $FeCl_2{\cdot}4H_2O$ (Acros Organics, 99+%) that was combined with 97.2 mL H_2O to form a solution. In Beaker 2, another solution was prepared by adding 1.60 g benzene-1,3,5-tricarboxylic acid (H_3BTC, Acros Organics, 98%) to 23.72 mL to 1 M solution of NaOH. The linker solution in Beaker 2 was then poured into Beaker 1 containing the Fe metal salt solution resulting in a green suspension. After approximately 6 h, the green suspension changed into a brown precipitate with no further color change observed after 24 h. Thereafter, washing of the precipitate was carried out with water and ethanol (3×) and the product was left to dry at room temperature.

2.3. Synthesis of Zr–BDC and Zr–BDC–NH_2

A previously published sustainable synthesis procedure was employed to synthesize Zr–BDC and Zr–BDC–NH_2.[15,18,29] 1.92 g of a Zr metal source *i.e.* $ZrOCl_2{\cdot}8H_2O$ (Sigma-Aldrich, 98%) was first dissolved in 28 mL H_2O in Beaker 1. Next, a solution was prepared by dissolving 1.03 g of H_2BDC (Acros Organics, 99+) for Zr–BDC synthesis, or the same amount of NH_2–H_2BDC (Sigma-Aldrich, 99%) for Zr–BDC–NH_2 synthesis, in 1 M NaOH in Beaker 2. Each linker solution was stirred for 30 min until it became clear. The metal salt solution was then mixed with each linker salt solution in separate beakers. This resulted in the immediate formation of a white precipitate for Zr–BDC and a yellow precipitate for Zr–BDC–NH_2. Following 24 h of stirring at room temperature, washing of the precipitate was performed with water and ethanol (3×) and the product was dried at room temperature. Fig. 1 illustrates the general scheme for the sustainable synthesis of MOFs, as described in Sections 2.1–2.3.

2.4. Characterization

Powder X-ray diffraction (PXRD) patterns of the synthesized MOFs were recorded employing a Philips X'PERT diffractometer having an X'Celerator detector (X'pert Pro PANalytical) equipped with Cu Kα radiation (λ = 0.15406 nm). The Fe–MIL-100 MOF mesoscopic order was probed using the low-angle PXRD mode. Fourier transform infrared (FTIR) spectra were obtained using a Bruker Alpha spectrometer equipped with a platinum attenuated total reflectance (ATR) sampling accessory. The spectra were recorded in the range of 4000–400 cm^{-1}. Thermogravimetric analysis (TGA) was performed to investigate the MOFs' stability using a PerkinElmer TGA 7 instrument. For

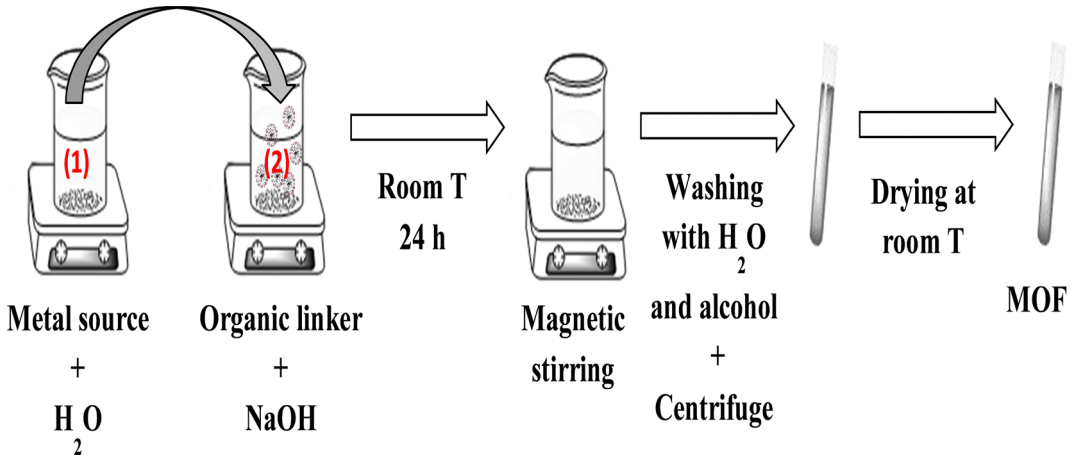

Fig. 1 Scheme for the sustainable synthesis of Al–MIL-53–NH_2, Fe–MIL-100 (solution 2 added to solution 1), Zr–BDC and Zr–BDC–NH_2.

the TGA analysis, the sample was heated from 25 to 900 °C at 20 °C min^{-1} in a flow of air. The N_2 adsorption/desorption isotherms were recorded at 77 K using a Micromeritics ASAP 2420 instrument. Before analysis, the samples were degassed for 16 h at 150 °C. The Brunauer–Emmett–Teller (BET) theory was used for specific surface area and porosity determination. The micropore/external surface area was calculated by the *t*-plot method and pore size distribution (PSD) by the Barrett–Joyner–Halenda (BJH) method on the N_2 adsorption branch corrected by the Kruk–Jaroniec–Sayari (KJS) method. The morphology of the MOFs was examined with a JEOL JSM-7500F field emission scanning electron microscope (FE-SEM). The samples were coated with carbon prior to SEM analysis. Transmission electron microscopy (TEM) images were recorded utilizing a JEOL 2100F instrument operating at 200 kV. For the TEM analysis, the samples were prepared by dispersing the MOF powder in ethanol, then the droplets of the suspension were placed on a Cu–carbon lacey grid, and dried at room temperature. H_2 and CO_2 adsorption/desorption measurements were performed with ultra-high purity gases using a Micromeritics 3Flex surface analyzer. Before gas sorption, the samples were degassed for 16 h at 150 °C.

3. Results and discussion

3.1. Phase purity and crystallinity

Fig. 2 displays the PXRD patterns of the sustainably synthesized MOFs compared to the simulated patterns of their conventionally synthesized counterparts (shown in black). Several simulated patterns exist for the Al–MIL-53 family of MOFs, which vary based on the flexibility of the MOF and the guest molecules present in the pores. These MOFs are isostructural with the aluminium dicarboxylate Al(OH)BDC, but their structures are altered by hydrogen bonding interactions between water molecules and linkers in the pores. In Fig. 2a, the PXRD pattern of the room temperature-synthesized Al–MIL-53–NH_2 is compared with the simulated pattern associated with CCDC code 220475 from the Cambridge Crystallographic Data Centre (CCDC).[30] The diffraction peaks from the simulated pattern are evident in the sustainably synthesized MOF, confirming its successful synthesis, albeit with variations in relative peak intensities and broadness. The synthesized Al–MIL-53–NH_2 shows similar crystal growth in both the (110) and (200) planes, whereas the simulated one has a preferential crystal growth in the (110) plane.[17,18] The broader peaks observed for the synthesized sample are due to the small crystallite size of the MOF as a result of the room temperature precipitation synthesis.[17] Typically, this MOF is distinguished by the presence of protonated carboxylate linkers that occupy its pores. These linker molecules are not readily removed by simple washing with water and ethanol without calcination. Since our Al–MIL-53–NH_2 MOF was synthesized at room temperature without calcination after washing, the presence of linker molecules in the pores is likely, a conclusion further supported by the TGA results.

Fe–MIL-100 is the iron(III) carboxylate built from the 1,3,5-benzenetricarboxylic acid (H_3BTC) linker and trimers of iron octahedra that share a common vertex μ–O. The high-angle (5–50°) and low-angle (1–6°) PXRD patterns of the room temperature synthesized Fe–MIL-100 are depicted in Fig. 2b and c, respectively. Both patterns perfectly align with the corresponding simulated pattern (CCDC 640536), with no detection of impurity peaks.[31] The room temperature synthesized Fe–MIL-100 MOF has the same phase and mesoscopic order as the conventional high temperature counterpart (simulated Fe–MIL-100). The mesoscopic order of the room temperature synthesized Fe–MIL-100 is apparent from the low-angle PXRD pattern, which displays peak positions and relative intensities that match those of the simulated pattern (Fig. 2c).

Zr–UiO-66 consists of a $Zr_6O_4(OH)_4$ cluster connected by H_2BDC linkers. The PXRD patterns of semi-crystalline Zr–BDC and Zr–BDC–NH_2 compared with the conventionally synthesized crystalline Zr–UiO-66 simulated pattern are displayed in Fig. 2d. A broad peak appears at the low 2-theta (2θ = 5–10°) region of the PXRD patterns for the room temperature synthesized Zr–BDC and Zr–BDC–NH_2. This low-angle peak occurs in the region where the typical peaks of Zr–UiO-66 are positioned, as seen in the simulated pattern of Zr–UiO-66 (CCDC 837796).[32] The immediate precipitate formation observed during the room

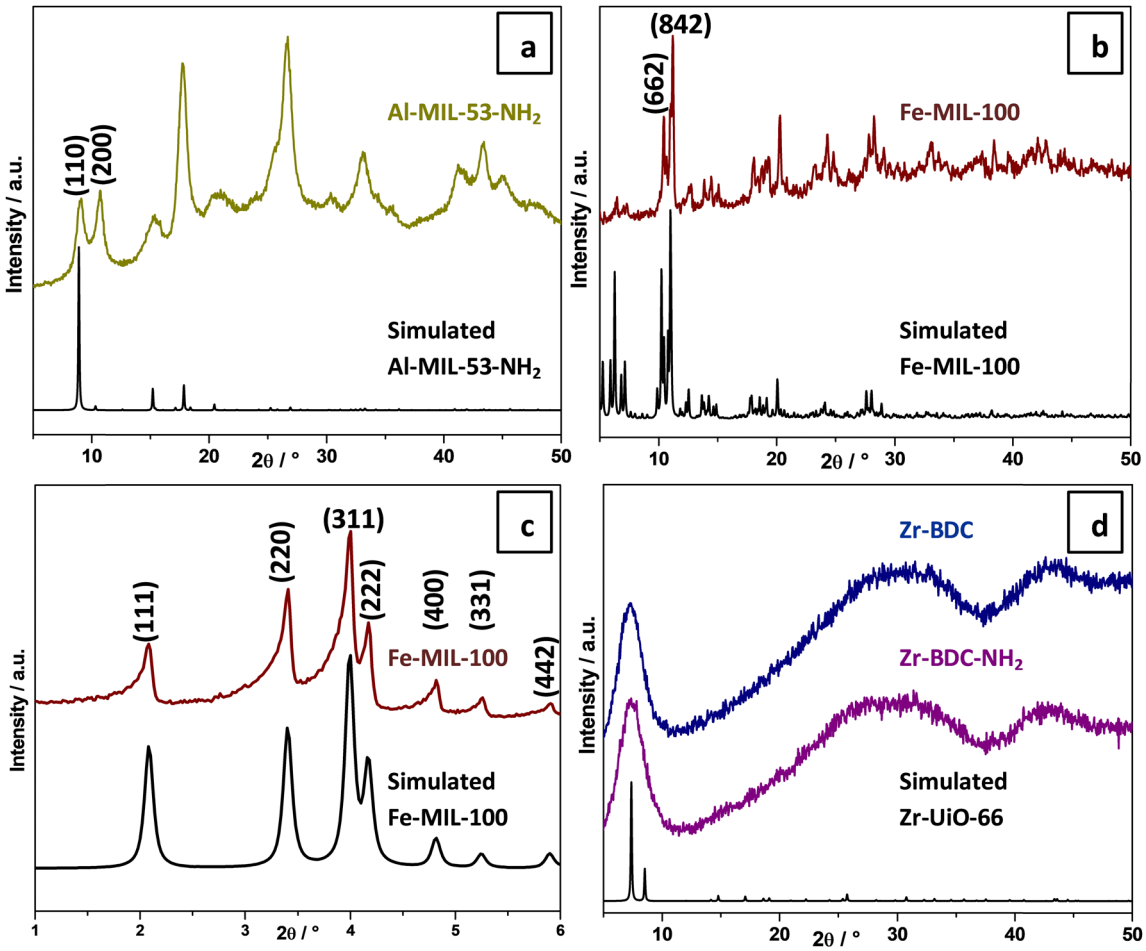

Fig. 2 PXRD patterns of (a) Al–NH_2–MIL-53, (b) Fe–MIL-100 (high angle), (c) Fe–MIL-100 (low angle), and (d) Zr–BDC and Zr–BDC–NH_2.

temperature synthesis of the MOFs, except for Fe–MIL-100 is the possible reason for the formation of MOFs with small domain sizes, as revealed by broad PXRD peaks.

3.2. Structural properties

FTIR spectroscopy was used to determine the bonding and functional groups in the MOFs. For all MOFs (Fig. 3a–d), the O–H stretching vibration was observed between 300 and 3700 cm^{-1}, and for Fe–MIL-100 (Fig. 3b), it is very broad. The presence of OH groups was expected due to the hygroscopic nature of MOFs, which readily adsorb moisture from the air.[30,33] Additionally, the drying process after the washing protocol might not have completely removed all the residual solvent from the MOF pores. C–H stretching bands occurred at 2980–2900 cm^{-1} for Al–MIL-53–NH_2 (Fig. 3a), Zr–BDC (Fig. 3c) and Zr–BDC–NH_2 (Fig. 3d) MOFs.[34] For all synthesized MOFs, the usual vibrational bands between 1400 and 1700 cm^{-1} are associated with coordinated carboxylate groups in MOFs.[30] Specifically, the bands at around 1552 and 1400 cm^{-1} correspond to the –COO asymmetric and –COO symmetric stretching vibrations of carboxylate groups, respectively.[30,35] The characteristic bands ascribed to metal–oxygen vibrations were observed for all MOFs in the region of 500–800 cm^{-1}.[30,33,36]

3.3. Thermal stability

The TGA plots of Al–MIL-53–NH_2, Fe–MIL-100 and the Zr-based MOFs are depicted in Fig. 4a, and the corresponding derivatives

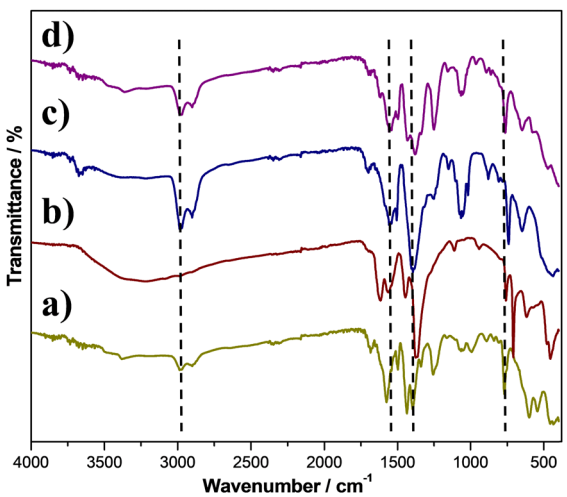

Fig. 3 FTIR spectra of (a) Al–NH_2–MIL-53, (b) Fe–MIL-100, (c) Zr–BDC and (d) Zr–BDC–NH_2.

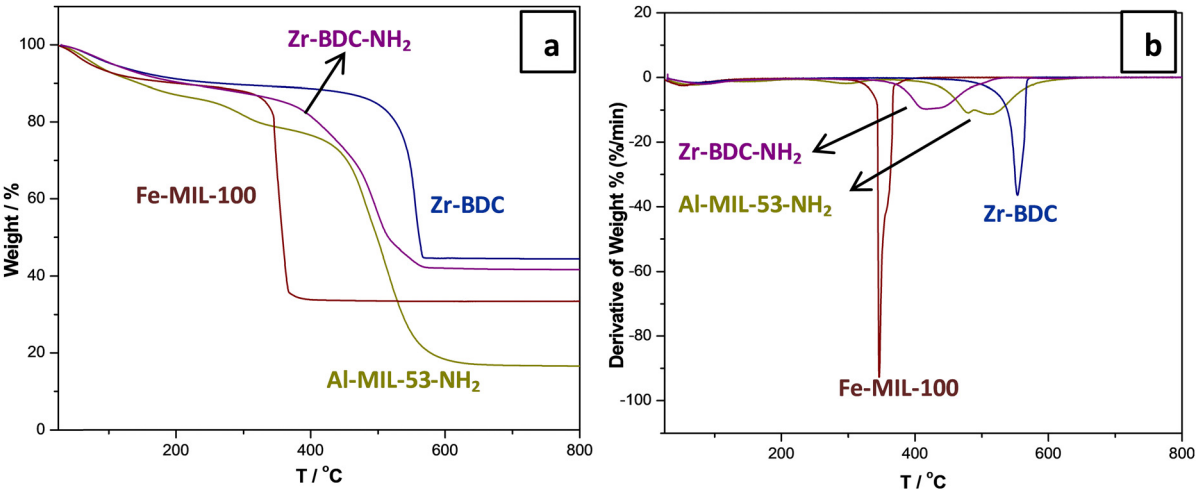

Fig. 4 (a) TGA and (b) DTG curves of Al–MIL-53–NH_2, Fe–MIL-100, Zr–BDC and Zr–BDC–NH_2.

are presented in Fig. 4b. Two distinct weight loss steps are observed. The initial weight loss below 150 °C for all the MOFs is due to solvent removal; in this case, it is due to the removal of either water from the synthesis and washing protocol or ethanol from the washing protocol. For Al–MIL-53–NH_2, the small weight loss at around 150–380 °C is most probably due to the residual protonated linker in the pores of the MOFs. This is in agreement with the PXRD results discussed above in relation to the selected simulated pattern (Fig. 2a). The second weight loss is attributed to the degradation of the MOF structure, and this is different for the four types of synthesized MOFs. It is obvious that Zr–BDC was the most stable MOF since the degradation of its structure started above 500 °C, as shown in Fig. 4b. This is supported by the Hard–Soft-Acid–Base theory; in this regard, Zr^{4+} in the metal clusters and O^{2-} in the carboxylate ligands form a strong bond resulting in a stable Zr–MOF.[37]

3.4. Morphology

The surface morphology of the prepared MOFs was examined using carbon-coated samples and the results are presented in Fig. 5. The synthesis at room temperature using water as a solvent resulted in the immediate precipitation of all the synthesized MOFs, with the exception of Fe–MIL-100. Hence, agglomeration was observed for Al–MIL-53–NH_2 as is evident in the FE-SEM micrograph in Fig. 5a and for the Zr–UiO-66 family of MOFs. The agglomerated particles arise from the clustering of small nanocrystals as confirmed by TEM images (Fig. 6a). For Fe–MIL-100, the FE-SEM image presents relatively well-formed octahedral-shaped crystals (Fig. 5b).[38] A similar observation has been reported for Fe–MIL-100 synthesized by a conventional approach.[39] The 6 h duration before the formation of the precipitate afforded well-formed larger crystals for Fe–MIL-100 compared to the other sustainably synthesized MOFs, as also revealed by the PXRD results (Fig. 2b).[18] No clear or distinct morphology is observed in the FE-SEM micrographs of Zr–BDC (Fig. 5c) and its amino-functionalized form, Zr–BDC–NH_2 (Fig. 5d). These results corroborate the observation by Yassin *et al.* for semi-crystalline UiO-66 type MOFs synthesized at room temperature with different solvent ratios.[29]

Fig. 6 presents the TEM micrographs of Al–MIL-53–NH_2 (a) and (b), Fe–MIL-100 (c) and (d) and Zr–BDC (e) and Zr–BDC–NH_2 (f). Agglomerated nanocrystals of Al–MIL-53–NH_2 are visible in Fig. 6a. The fast precipitation of Al–MIL-53–NH_2 during the room temperature synthesis creates small pores attributed to intercrystalline mesoporosity, as displayed with white arrows in Fig. 6b.[17] The TEM images of Fe–MIL-100 in Fig. 6c and d show clean surface edges and a comparatively well-formed morphology of the MOF.[18] The fast degradation of MOFs in an electron beam complicates the acquisition of TEM images for Fe–MIL-100, as exhibited in Fig. 6c and d, for further clarification of the MOF morphology. For Zr–BDC (Fig. 6e) and Zr–BDC–NH_2 (Fig. 6f), the TEM images confirm very small aggregates of MOFs with no definite shapes, consistent with the large domains observed in the FE-SEM images of the same MOFs (Fig. 5c and d).

3.5. Textural properties

Textural properties of the four types of MOFs were determined using N_2 adsorption/desorption isotherms at 77 K (Fig. 7). The N_2 adsorption/desorption isotherm for Al–MIL-53–NH_2 (Fig. 7a) exhibits a shape resembling a Type IV(a) isotherm, according to the IUPAC classification. This suggests partially blocked microporosity resulting from the presence of protonated linkers in the pores of the MOF.[22,28] A hysteresis loop (Type H2) beginning at relative pressures (p/p_0) typically greater than 0.4 is characteristic of this type of isotherm, and it is associated with mesoporosity.[17] Type H2 hysteresis is characteristic of channels with a pore opening smaller than the pore body. The PSD plot shows a pore diameter in the mesoporous range centred around 8 nm (Fig. 7b). The mesopores are due to the intercrystalline voids, which are formed during the fast precipitation at room temperature in the synthesis of MOFs in water. The formed mesopores in the agglomerated MOFs are also detected

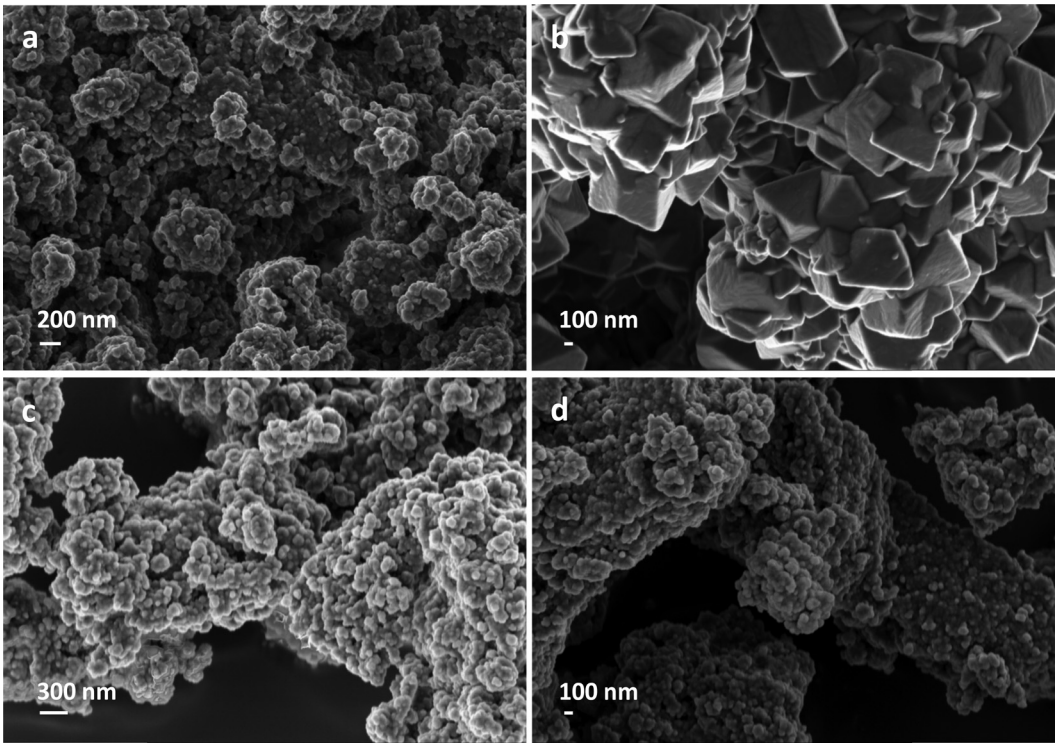

Fig. 5 SEM images of (a) Al–MIL-53–NH_2, (b) Fe–MIL-100, (c) Zr–BDC and (d) Zr–BDC–NH_2.

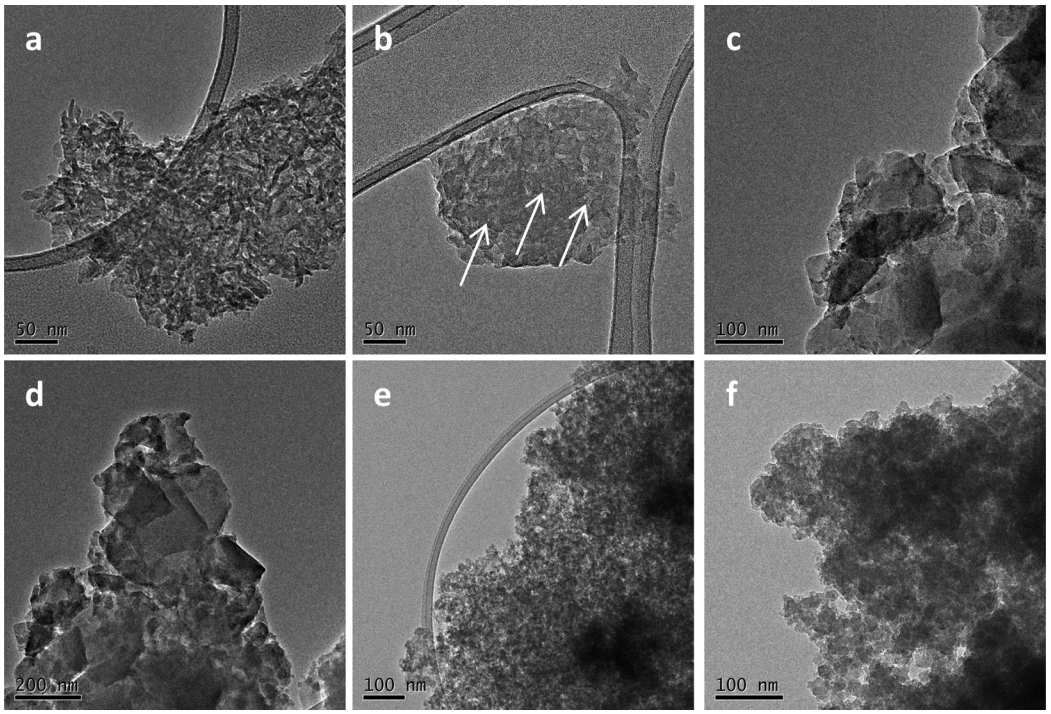

Fig. 6 TEM images of Al–MIL-53–NH_2 (a) and (b), Fe–MIL-100 (c) and (d), and Zr–BDC (e) and Zr–BDC–NH_2 (f).

in the TEM images shown in Fig. 7b. Molina *et al.*[17] reported similar textural properties for Al–MIL-53–NH_2 synthesized in water at room temperature.

A typical Type I isotherm from the IUPAC classification, which is consistent with the microporosity was exhibited by Fe–MIL-100 (Fig. 7c). This isotherm type has also been observed in

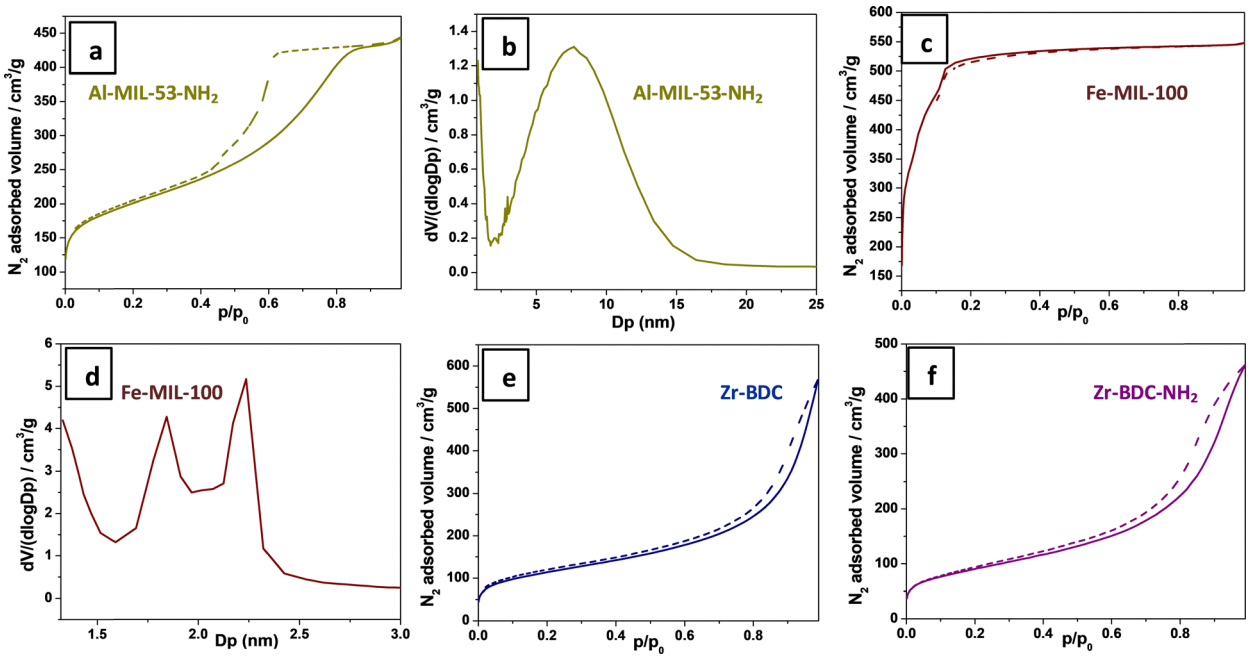

Fig. 7 (a) N_2 adsorption/desorption isotherm and the (b) PSD curve for Al–MIL-53–NH_2, (c) N_2 adsorption/desorption isotherm and the (d) PSD curve for Fe–MIL-100, and the N_2 adsorption/desorption isotherms for (e) Zr–BDC and (f) Zr–BDC–NH_2.

conventionally synthesized Fe–MIL-100.[31] The PSD curve from the adsorption branch of the isotherm depicts two peaks at 1.8 and 2.2 nm (Fig. 6d), which indicates mesocavities in Fe–MIL-100. Fe–MIL-100 materials have well-known mesocages with diameters of 2.5 and 2.9 nm.[23,31] Each of these values is 0.7 nm larger than the estimated diameters of the respective mesocages in this work. The small mesocavities in the PSD curve can be explained by the fact that the BJH method is known to underestimate the pore size even when amended by the KJS method, which is applied to MCM-41 (MCM = mobil composition of matter) type materials.[40] The BJH underestimation has been reported for Fe–MIL-100[23,31] and Fe–MIL-101 MOFs.[41] The BET surface area obtained for Fe–MIL-100 was 2013 $m^2\ g^{-1}$ (Table 1), and it is among the high values reported in the literature (Table 2). The capacity of ethanol to eliminate water-soluble and organic residues may have enhanced the surface areas of Fe–MIL-100 and Al–MIL-53–NH_2 MOFs. The TGA graphs shown in Fig. 4a indicate that the structures of the MOFs remained unaffected by ethanol washing. Additionally, the water/ethanol washing protocol presents a more environmentally friendly option.

Fig. 7e and f display the N_2 adsorption/desorption isotherms for Zr–BDC and Zr–BDC–NH_2, respectively. The isotherms exhibit some features that align with the IUPAC Types IV and II physisorption classification.[29] However, the final saturation plateau characteristic of a Type IV isotherm is absent. A hysteresis loop (Type H3) is present, which is not characteristic of a Type II isotherm. Type H3 hysteresis is associated with a very wide distribution of pore sizes. The small hysteresis loop can be attributed to the void spaces between aggregated particles, as illustrated in the SEM (Fig. 5c and d) and TEM (Fig. 6e and f) images. The UiO-66 types (Zr–BDC and Zr–BDC–NH_2) exhibited significantly lower surface areas (415 and 330 $m^2\ g^{-1}$, respectively) in comparison to Fe–MIL-100 (2013 $m^2\ g^{-1}$) and Al–MIL-53–NH_2 (850 $m^2\ g^{-1}$). The BET surface areas are also less than that of conventionally synthesized UiO-66 MOF; a BET surface area of 1069 $m^2\ g^{-1}$ was reported for the latter.[32] The room temperature synthesis in water, conducted without a modulator, led to the uncontrolled assembly of large domains, resulting in semi-crystalline materials. This incomplete crystallization is evident from the PXRD analysis (Fig. 2d) and the particle aggregations observed in the SEM (Fig. 5c and d) and

Table 1 Textural properties, and H_2 and CO_2 uptakes for synthesized MOFs

Sample name	S_{BET}[a] ($m^2\ g^{-1}$)	S_{micro}[b] ($m^2\ g^{-1}$)	Vp[c] ($cm^3\ g^{-1}$)	Dp[d] (nm)	H_2[e] (wt%)	CO_2[f] (wt%)
Al–MIL-53–NH_2	850 ± 0.92	407	0.82	8.0	0.5	4.5
Fe–MIL-100	2013 ± 1.00	1372	0.89	1.8, 2.2	1.0	8.5
Zr–BDC	415 ± 0.39	58.4	0.81	—	0.4	2.1
Zr–BDC–NH_2	330 ± 0.42	17.3	0.69	—	0.3	2.3

[a] BET surface area ± standard error. [b] Micropore area from the *t*-plot. [c] Total pore volume measured at $p/p_0 = 0.98$. [d] Pore size from PSD derived using the BJH method applied to the adsorption branch, corrected by the KJS method. [e] H_2 uptake at 77 K and 1 bar and [f] CO_2 adsorbed at 298 K and 1 bar.

Table 2 H_2 and CO_2 uptakes for Fe–MIL-100 MOFs synthesized in this work and from the literature

Sample name	S_{BET}[a] (m^2 g^{-1})	Synthesis method	H_2[b] (wt%)	CO_2[c] (wt%)	Ref.
Fe–MIL-100	2013	Sustainable	1.0	8.5	This work
Fe–MIL-100	2001	Sustainable	0.75[d]	—	47
Fe–MIL-100	1350	Commercial	0.85	—	48
Fe–MIL-100–H_2	790	Hydrothermal	—	4.4	49
Fe–MIL-100	2200	Hydrothermal	—	8.5	50

[a] S_{BET} is the BET surface area. [b] H_2 uptake at 77 k and 1 bar. [c] CO_2 uptake at 298 K and 1 bar. [d] Measured at 298 K and 50 bar.

TEM (Fig. 6e and f) images. Consequently, this is the primary reason for the low microporosity and surface areas of the room temperature, water-synthesized Zr–BDC and Zr–BDC–NH_2 MOFs.[15]

3.6. H_2 and CO_2 storage measurements

The H_2 uptake of the MOFs was determined at 77 K and plotted as H_2 uptake (wt%) vs pressure (bar) in Fig. 8a. Among the four MOFs, Fe–MIL-100 exhibits the highest H_2 uptake of 1.0 wt% at 77 K and 1 bar (Table 1). Meanwhile, Al–MIL-53–NH_2, Zr–BDC and Zr–BDC–NH_2 exhibit H_2 uptakes of 0.5, 0.4 and 0.3 wt%, respectively. Table 1 further illustrates that the H_2 uptake of the MOFs is directly proportional to the BET surface area and micropore surface area. It has also been reported that hydrogen adsorption is favorable in MOFs with a high pore volume as confirmed in Table 1.[42] The hydrogen adsorption is fully reversible for all the MOFs (Fig. 8a). This is expected since H_2 uptake in porous materials like MOFs occurs by weak van der Waals attraction underpinning physical adsorption.[43] Furthermore, the hydrogen adsorption curve does not reach saturation for all the MOFs and this is most pronounced for Fe–MIL-100. This indicates that at higher pressures, higher hydrogen uptake will be attained for these materials. The sustainably synthesized Fe–MIL-100 was revealed to contain small mesopores. The presence of small mesopores is known to favour H_2 uptake at higher pressures for MOFs.[44]

The CO_2 uptake of the MOFs is depicted in Fig. 8b plotted as CO_2 uptake (wt%) vs pressure (bar) at 298 K. Fe–MIL-100, Al–MIL-53–NH_2, Zr–BDC–NH_2 and Zr–BDC exhibited CO_2 uptakes of 8.5, 4.5, 2.3 and 2.1 wt%, respectively. Similar to the H_2 uptake, there was a general correlation between CO_2 uptake and the BET surface area, micropore area and pore volume. However, Zr–BDC–NH_2 with a lower surface area than Zr–BDC has a higher CO_2 uptake than Zr–BDC. This observation is linked to the existence of amino groups in Zr–BDC–NH_2, which might have additional affinity for CO_2 *via* Lewis acid–base interactions, where the lone pair of electrons on the nitrogen can interact with the electrophilic carbon atoms of CO_2. In this regard, amino groups may also have contributed to the high CO_2 uptake in Al–MIL-53–NH_2 in addition to its high surface area.[45,46]

Table 2 shows a comparison of the BET surface area, and H_2 and CO_2 storage for commercial Fe–MIL-100, hydrothermally synthesized Fe–MIL-100 and sustainably synthesized Fe–MIL-100. It can be seen that our sustainably synthesized sample has a higher BET surface area compared to the Fe–MIL-100 synthesized in a similar fashion from the literature.[47] Orcajo *et al.* used commercial Fe–MIL-100 with the name KRICT F100 for H_2 storage at 1 bar and 77 K, and obtained 0.85 wt% H_2 storage, which is lower than the value attained for the sustainably synthesized Fe–MIL-100 in this work.[48] In another study, a hydrothermally synthesized sample that had been heat treated in a flow of H_2, denoted as H_2–Fe–MIL-100, adsorbed 4.4 wt% CO_2 at 298 K and 1 bar,[49] which is much lower than the CO_2 uptake amount achieved for Fe–MIL-100 synthesized in this work. Meanwhile, hydrothermally synthesized Fe–MIL-100 with a surface area of 2200 m^2 g^{-1} and a pore volume of 1.07 cm^3 g^{-1} stored a similar amount of CO_2 to the sustainably synthesized Fe–MIL-100 with a pore volume of 0.89 cm^3 g^{-1}.[50] Activation temperature also plays a vital role in gas adsorption.[42,50]

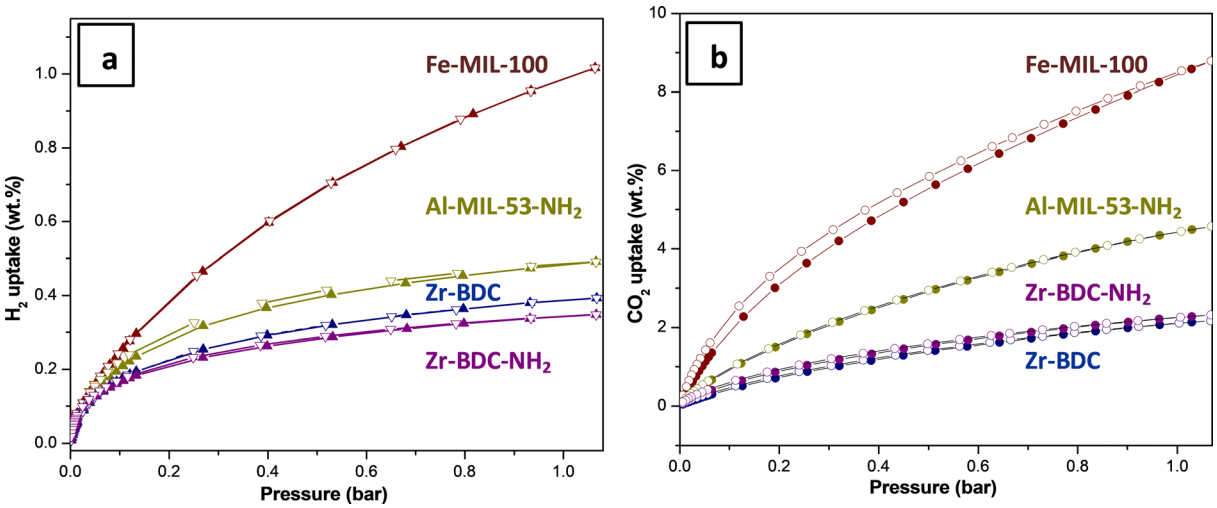

Fig. 8 (a) H_2 isotherms at 77 K and (b) CO_2 isotherms at 298 K for Al–MIL-53–NH_2, Fe–MIL-100, Zr–BDC and Zr–BDC–NH_2. Closed symbols are for adsorption and open symbols are for desorption.

According to Vo *et al.*, the high activation temperature resulted in high CO_2 adsorption by increasing the porosity of the MOFs.[50] This was confirmed for the hydrothermally synthesized Fe–MIL-100[50] and the room temperature synthesized Fe–MIL-100 in this work. At low pressure, CO_2 molecules are adsorbed favourably in micropores. Both the hydrothermal and room temperature synthesized samples show similar microporosity which resulted in similar CO_2 uptake at 1 bar. This is achieved despite the hydrothermally synthesized Fe–MIL-100 having a slightly higher surface area and pore volume. Overall, these results demonstrate the potential of sustainably synthesized Fe–MIL-100 for gas storage applications.

4. Conclusion

Al–MIL-53–NH_2, Fe–MIL-100 and Zr-based MOFs (Zr–BDC and Zr–BDC–NH_2) were successfully synthesized at room temperature using water as the solvent. The PXRD patterns of the sustainably synthesized MOFs were mostly consistent with the simulated patterns derived from conventionally synthesized MOFs. For Fe–MIL-100, matching peak positions and intensities were observed and the MOF exhibited a high degree of crystallinity. Al–MIL-53–NH_2 was obtained as a nanocrystalline MOF, confirmed by broad PXRD peaks. Zr–BDC and Zr–BDC–NH_2 were revealed as semi-crystalline and part of the UiO-66 family of MOFs. Morphological analysis showed Fe–MIL-100 to consist of octahedral-shaped crystals. Fast nucleation due to instantaneous precipitation during the synthesis of Al–MIL-53–NH_2, Zr–BDC and Zr–BDC–NH_2 afforded agglomerated MOF particles. All the synthesized MOFs were porous with BET surface areas ranging from 330 to 2013 $m^2\ g^{-1}$. Fe–MIL-100 displayed the highest H_2 and CO_2 storage at 77 K and 298 K, respectively, at 1 bar pressure. The highest BET surface area obtained for Fe–MIL-100 contributed to the highest uptake of gases. While H_2 uptake followed the order Fe–MIL-100 > Al–MIL-53–NH_2 > Zr–BDC > Zr–BDC–NH_2, the least CO_2 uptake was obtained for Zr–BDC. This work has demonstrated the potential of these selected sustainably synthesized MOFs for H_2 and CO_2 storage.

Author contributions

Nejat Redwan Habib: conceptualization, methodology, formal analysis, investigation, validation, and writing – original draft. Isabel Diaz: resources and writing – review & editing. Abi M. Taddesse: resources and writing – review & editing. Henrietta W. Langmi: conceptualization, methodology, funding acquisition, project administration, resources, supervision, validation, and writing – review & editing.

Conflicts of interest

There are no conflicts to declare.

Data availability

The experimental data that support the findings of this study will be available upon request.

Acknowledgements

We thank the Department of Science, Technology and Innovation (DSTI) and the National Research Foundation (NRF) South African Research Chairs Initiative (SARChI) (Grant Number: 2090155358). The NRF CPRR funding stream (Grant Number: 0215586378) is also acknowledged. NRH acknowledges the University of Pretoria for post-doctoral researcher funding. ID acknowledges funding from the MCIN/AEI under grant code: PID2022-136321OB-C21/AEI/10.13039/501100011033/FEDER, UE. This research work was also financially supported by Haramaya University (HURG-2020-03-02-75), Ethiopia.

References

1 P. Liu, Y. Jia, Y. Ning, X. Zhang, S. Tian, F. Yang, W. Song and Y. Zhang, *Int. J. Hydrogen Energy*, 2024, **56**, 315–322, DOI: 10.1016/j.ijhydene.2023.12.178.
2 S. Choi, J. H. Drese and C. W. Jones, *ChemSusChem*, 2009, **2**, 796–854, DOI: 10.1002/cssc.200900036.
3 M. S. Zantye, A. Arora and M. M. F. Hasan, *Energy Environ. Sci.*, 2021, **14**, 3986–4008, DOI: 10.1039/D0EE03946B.
4 D. DeSantis, J. A. Mason, B. D. James, C. Houchins, J. R. Long and M. Veenstra, *Energy Fuels*, 2017, **31**, 2024–2032, DOI: 10.1021/acs.energyfuels.6b02510.
5 S. E. Bambalaza, H. W. Langmi, R. Mokaya, N. M. Musyoka, J. Ren and L. E. Khotseng, *J. Mater. Chem. A*, 2018, **6**, 23569–23577, DOI: 10.1039/C8TA09227C.
6 A. A. Elhussien, I. Abdulazeez, H. Alasiri and W. A. Fouad, *Microporous Mesoporous Mater.*, 2025, **384**, 113442, DOI: 10.1016/j.micromeso.2024.113442.
7 S. Elyasi, S. Saha, N. Hameed, P. J. Mahon, S. Juodkazis and N. Salim, *Int. J. Hydrogen Energy*, 2024, **62**, 272–306, DOI: 10.1016/j.ijhydene.2024.02.337.
8 T. R. Menezes, K. M. C. Santos, H. Mao, K. Santos, J. F. De Conto, J. A. Reimer, S. M. E. Dariva and C. C. Santana, *Sep. Purif. Technol.*, 2025, **354**, 129033, DOI: 10.1016/j.seppur.2024.129033.
9 Z. Zheng, A. H. Alawadhi and O. M. Yaghi, *Mol. Front. J.*, 2023, **07**, 20–39, DOI: 10.1142/S2529732523400011.
10 M. A. Abdelkareem, Q. Abbas, E. T. Sayed, N. Shehata, J. B. M. Parambath, A. H. Alami and A. G. Olabi, *Energy*, 2024, **299**, 131127, DOI: 10.1016/j.energy.2024.131127.
11 C. Gunathilake, I. Soliman, D. Panthi, P. Tandler, O. Fatani, N. A. Ghulamullah, D. Marasinghe, M. Farhath, T. Madhujith, K. Conrad, Y. Du and M. Jaroniec, *Chem. Soc. Rev.*, 2024, **53**, 10900–10969, DOI: 10.1039/d3cs00731f.
12 M. Akmal, M. A. Iqbal, T. H. Mawat, H. K. R. AL-Sharifi, G. Iram, A. Majeed, M. Yaqoob and M. Atif, *Inorg. Chem. Commun.*, 2025, **175**, 114105, DOI: 10.1016/j.inoche.2025.114105.

13 F. zohra Zeggai, Z. Ait-Touchente, K. Bachari and A. Elaissari, *Chem. Phys. Impact*, 2025, **10**, 100864, DOI: 10.1016/j.chphi.2025.100864.
14 T. J. Azbell, T. A. Pitt, R. T. Jerozal, R. M. Mandel and P. J. Milner, *Acc. Mater. Res.*, 2023, **4**, 867–878, DOI: 10.1021/accountsmr.3c00121.
15 N. Redwan Habib, A. M. Taddesse, R. Sainz, M. Sánchez-Sánchez and I. Díaz, *J. Photochem. Photobiol., A*, 2024, **456**, 115842, DOI: 10.1016/j.jphotochem.2024.115842.
16 N. Getachew, Y. Chebude, I. Díaz and M. Sánchez-Sánchez, *J. Porous Mater.*, 2014, **21**, 769–773, DOI: 10.1007/s10934-014-9823-6.
17 M. A. Molina, N. R. Habib, I. Díaz and M. Sánchez-Sánchez, *Catal. Today*, 2022, **394–396**, 117–124, DOI: 10.1016/j.cattod.2021.10.019.
18 N. R. Habib, R. Sainz, A. M. Taddesse and I. Díaz, *Catal. Today*, 2022, **390–391**, 316–325, DOI: 10.1016/j.cattod.2021.09.028.
19 T. Kundu, B. B. Shah, L. Bolinois and D. Zhao, *Chem. Mater.*, 2019, **31**, 2842–2847, DOI: 10.1021/acs.chemmater.8b05332.
20 F. Martínez, G. Orcajo, D. Briones, P. Leo and G. Calleja, *Microporous Mesoporous Mater.*, 2017, **246**, 43–50, DOI: 10.1016/j.micromeso.2017.03.011.
21 K. Mosupi, M. Masukume, G. Weng, N. M. Musyoka and H. W. Langmi, *Coord. Chem. Rev.*, 2025, **529**, 216467, DOI: 10.1016/j.ccr.2025.216467.
22 N. R. Habib, E. Asedegbega-Nieto, A. M. Taddesse and I. Díaz, *Dalton Trans.*, 2021, **50**, 10340–10353, DOI: 10.1039/D1DT01531A.
23 K. Guesh, C. A. D. Caiuby, Á. Mayoral, M. Díaz-García, I. Díaz and M. Sánchez-Sánchez, *Cryst. Growth Des.*, 2017, **17**, 1806–1813, DOI: 10.1021/acs.cgd.6b01776.
24 V. R. Bakuru, S. R. Churipard, S. P. Maradur and S. B. Kalidindi, *Dalton Trans.*, 2019, **48**, 843–847, DOI: 10.1039/C8DT03512A.
25 A. Hadush, T. Kebede, A. M. Taddesse, N. R. Habib and M. Sánchez-Sánchez, *Opt. Mater.*, 2024, **155**, 115901, DOI: 10.1016/j.optmat.2024.115901.
26 Y. Qi, Y. Luan, X. Peng, M. Yang, J. Hou and G. Wang, *Eur. J. Inorg. Chem.*, 2015, 5099–5105, DOI: 10.1002/ejic.201500808.
27 S. Zhang, L. Zhou and M. Chen, *RSC Adv.*, 2018, **8**, 12282–12291, DOI: 10.1039/C8RA01507D.
28 M. Sánchez-Sánchez, N. Getachew, K. Díaz, M. Díaz-García, Y. Chebude and I. Díaz, *Green Chem.*, 2015, **17**, 1500–1509, DOI: 10.1039/C4GC01861C.
29 J. M. Yassin, A. M. Taddesse and M. Sánchez-Sánchez, *Inorganics*, 2025, **13**, 131, DOI: 10.3390/inorganics13050131.
30 T. Loiseau, C. Serre, C. Huguenard, G. Fink, F. Taulelle, M. Henry, T. Bataille and G. Férey, *Chem. – Eur. J.*, 2004, **10**, 1373–1382, DOI: 10.1002/chem.200305413.
31 P. Horcajada, S. Surblé, C. Serre, D. Hong, Y. Seo, J. Chang, J.-M. Grenèche, I. Margiolaki and G. Férey, *Chem. Commun.*, 2007, 2820–2822, DOI: 10.1039/b704325b.
32 L. Valenzano, B. Civalleri, S. Chavan, S. Bordiga, M. H. Nilsen, S. Jakobsen, K. P. Lillerud and C. Lamberti, *Chem. Mater.*, 2011, **23**, 1700–1718, DOI: 10.1021/cm1022882.
33 T. T. K. Ngan Tran, H. L. Ho, H. V. Nguyen, B. T. Tran, T. T. Nguyen, P. Q. Thi Bui and L. G. Bach, *Open Chem.*, 2022, **20**, 52–60, DOI: 10.1515/chem-2021-0110.
34 R. A. Espinosa-Flores, M. D. Trejo-Valdez, M. E. Manríquez-Ramírez and F. J. Tzompantzi-Morales, *Heliyon*, 2023, **9**, e17138, DOI: 10.1016/j.heliyon.2023.e17138.
35 H. R. Abid, Z. H. Rada, J. Shang and S. Wang, *Polyhedron*, 2016, **120**, 103–111, DOI: 10.1016/j.poly.2016.06.034.
36 J. M. Yassin, A. M. Taddesse and M. Sánchez-Sánchez, *Catal. Today*, 2020, **390–391**, 162–175, DOI: 10.1016/j.cattod.2021.11.037.
37 K. O. Kirlikovali, S. L. Hanna, F. A. Son and O. K. Farha, *ACS Nanosci. Au*, 2023, **3**, 37–45, DOI: 10.1021/acsnanoscienceau.2c00046.
38 D. T. Tran, T. D. To, T. H. Le, Q. T. Dao and L. D. Nghiem, *J. Ind. Eng. Chem.*, 2025, **147**, 149–160, DOI: 10.1016/j.jiec.2024.12.009.
39 M. A. Simon, E. Anggraeni, F. E. Soetaredjo, S. P. Santoso, W. Irawaty, T. C. Thanh, S. B. Hartono, M. Yuliana and S. Ismadji, *Sci. Rep.*, 2019, **9**, 6907, DOI: 10.1038/s41598-019-53436-3.
40 M. Sanchez-Sanchez, I. De Asua, D. Ruano and K. Díaz, *Cryst. Growth Des.*, 2015, **15**, 4498–4506, DOI: 10.1021/acs.cgd.5b00755.
41 J. G. Flores, R. Delgado-García and M. Sánchez-Sánchez, *Catal. Today*, 2022, **390–391**, 237–245, DOI: 10.1016/j.cattod.2021.11.004.
42 V. Zeleňák and I. Saldan, *Nanomaterials*, 2021, **11**, 1638, DOI: 10.3390/nano11071638.
43 H. W. Langmi, J. Ren, B. North, M. Mathe and D. Bessarabov, *Electrochim. Acta*, 2014, **128**, 368–392, DOI: 10.1016/j.electacta.2013.10.190.
44 S. E. Bambalaza, H. W. Langmi, R. Mokaya, N. M. Musyoka and L. E. Khotseng, *Int. J. Hydrogen Energy*, 2021, **46**, 8607–8620, DOI: 10.1016/j.ijhydene.2020.12.049.
45 J. Senith Ravishan Fernando, S. S. Asaithambi and S. Maruti Chavan, *ChemPlusChem*, 2024, **89**, e202400107, DOI: 10.1002/cplu.202400107.
46 B. Petrovic, M. Gorbounov and S. Masoudi Soltani, *Carbon Capture Sci. Technol.*, 2022, **3**, 100045, DOI: 10.1016/j.ccst.2022.100045.
47 C. Liu, D. Shen, Z. Tu and S. Li, *Int. J. Hydrogen Energy*, 2022, **47**, 5393–5402, DOI: 10.1016/j.ijhydene.2021.11.168.
48 G. Orcajo, H. Montes-Andrés, J. A. Villajos, C. Martos, J. A. Botas and G. Calleja, *Int. J. Hydrogen Energy*, 2019, **44**, 19285–19293, DOI: 10.1016/j.ijhydene.2018.03.151.
49 P. Teerachawanwong, W. Dilokekunakul, P. Phadungbut, N. Klomkliang, S. Supasitmongkol, S. Chaemchuen and F. Verpoort, *Fuel*, 2023, **331**, 125863, DOI: 10.1016/j.fuel.2022.125863.
50 T. K. Vo, Y. S. Bae, B. J. Chang, S. Y. Moon, J. H. Kim and J. Kim, *Microporous Mesoporous Mater.*, 2019, **274**, 17–24, DOI: 10.1016/j.micromeso.2018.07.024.